Electromagnetic Characteristics and Modal Analysis of Multi-DOF Motors With Air-Floation

ZHENG LI, (Member, IEEE), LIBO LIU, XUANXUAN XING, ZHIBANG YAN, YU LIU, AND HEXU SUN, (Senior Member, IEEE)
School of Electrical Engineering, Hebei University of Science and Technology, Shijiazhuang, Hebei 050018, China

Corresponding authors: Zheng Li (lzhfgd@163.com) and Hexu Sun (sunhxhb@outlook.com)

ABSTRACT In this paper, based on the multi-DOF motor, the structure is optimized and gas lubricated bearings are added, and the structure of the multi-of motor is proposed. Firstly, the basic structure and working principle of the motor are described. Through the analytical calculation and frequency decomposition of the electromagnetic force, the magnetic density cloud diagram and the magnetic field vector diagram of the air-floating multi-DOF motor (AMM) at the rated speed are analyzed. The variation of radial electromagnetic force (REF) with horizontal circumferential space is solved. The changes of electromagnetic force under different deflection angles and different air gap distances are calculated. Through the modal analysis of the stator and rotor of the air floating multi-degree of freedom motor, the deformation under the natural frequency is obtained by using the finite element software, and the influence of the stator material on the modal analysis is explored. It provides new ideas for the design of multi-DOF motors.

INDEX TERMS Multi-DOF motor, gas lubrication, electromagnetic properties, finite element analysis, radial electromagnetic force, modal analysis.

I. INTRODUCTION

With the innovation of AC motors and the continuous due to the unceasing development and progress of science and technology, the traditional manufacturing industry began to transform, and high-end manufacturing has begun to emerge. At this time, there is an urgent need for the further development of high-efficiency, high-precision and low-energy motors [1]–[3]. Traditional motors can't meet the current manufacturing industry, and there has been an update in the motor industry. The emergence of multi-degree-of-freedom motors replaces multiple single-degree-of-freedom transmission structures, avoiding the reduction of transmission efficiency and transmission accuracy caused by complex transmission structures [4]–[7].

In the process of lubrication technology development, gas lubrication technology compared with the past few years of development by leaps and bounds, this lubrication mode not only has the advantage of low friction coefficient, but also

The associate editor coordinating the review of this manuscript and approving it for publication was Qinfen Lu.

can be applied to a wide range of conditions, and began to attract people's attention. Compared with rolling bearings and oil film lubrication, gas lubrication has enhanced transmission precision, operating life and stabilizing performance [8]–[11], while the power consumption goes down. Consequently, gas bearings are gradually favored by people and become a major part in the contactless support area [12]–[14]. Now we combine the air bearing with the multi-degree-of-freedom motor, forming a new motor model, namely the AMM structure, which combines the advantages of the two. This new type of motor realizes the transform of driving method, and it will more superior than the traditional multi-degree-of-freedom motor performance.

In terms of high-speed electric drive motors, bearings with long life and low wear need to be selected at high speeds. Gas bearings have the characteristics of system integration and high load capacity, and stand out in industrial applications [15], [16]. The turbogenerator has a complex turbocharger mechanism, and the gas bearing can meet the requirements of low pollution, wide temperature scheduling and high stability, and has been favored by industrial applications [17], [18].

In the literature [19], the gas effect, roughness effect and edge leakage effect of the gas dynamic bearing were analyzed, and the influence of the static bearing capacity of the gas bearing was analyzed by the dynamic analysis method. The friction torque measured when the gas bearing is working will cause torque unbalance. The sensor can be installed on the rotor to realize the co-rotation of the sensor and the rotor to calculate the friction torque [20]. As a substitute for the current traditional bearing, the magnetic-air hybrid bearing can meet the needs of a large number of turbomachinery, but the stability has been strictly tested [21]–[23]. When simulating the static characteristics of a gas bearing, theoretically, the coupling effect can be solved by the finite element method for multiple boundary conditions through the Reynolds equation. For the operation of the gas-bearing multi-degree-of-freedom motor, the gas film formed by the bearing will be affected during the motor rotor support process and the electromagnetic operation process [24], [25]. Therefore, when the whole motor is powered on, the electromagnetic excitation will cause different degrees of resonance to the motor, and the stability of the air film bearing will be affected [26], [28]. By testing and analyzing the oscillating movement property of the electric machine stator, the law of resonance caused by the motor can be found, the faulty operation of the gas bearing can be avoided, and the design requirements of stable operation can be completed [29], [30].

The structural model of the AMM proposed in this paper is explained, and the fundamental operating principle of the electrical machine is described. Finite element software was used to analyze and calculate the electromagnetic field of the motor. In addition, the magnetic field distribution during the movement process is obtained by the analytical method, The REF changes with the horizontal circular space are solved, and the variation of electromagnetic interaction force at various deflection angles and different air gap distances are calculated. In this paper, we use finite element software to perform modal dissection of the motor to simulate the modal deformation of the rotor. Then this paper explores the influence of stator material on the modal analysis and obtains the distribution clouds at the intrinsic frequency and the deformation under the mode to provide a reference for the prevention of motor resonance. The combination of multi-degree-of-freedom motors and gas lubrication technology is in line with the forward trend of motors.

II. MOTOR STRUCTURE AND WORKING PRICIPLE

The AMM structure combines the advantages of multi-degree-of-freedom motors and gas lubrication and can be applied to high-precision multi-directional rotary motion. During the operation of the motor, the rotor is in a suspended state, and the stator and rotor have no contact, which minimizes the friction of the rotor during rotation. AMM effectively improves the problems of large weight and volume, low precision, complex control, and large friction loss of the motor. In the figure, the air supply pipeline is connected to the external air source and is transported to the

TABLE 1. Paramenters of the AMM.

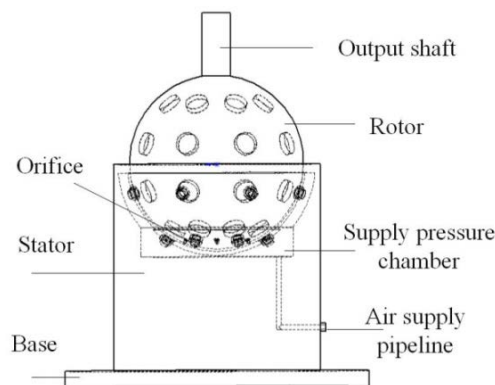| Parameter	Value
Rated power P/kW	2
Rated speed n/rpm	1500
Maximum deflection angle α max (°)	150
Turn Ratio	100
Phase number	3
Rated frequency f/Hz	125

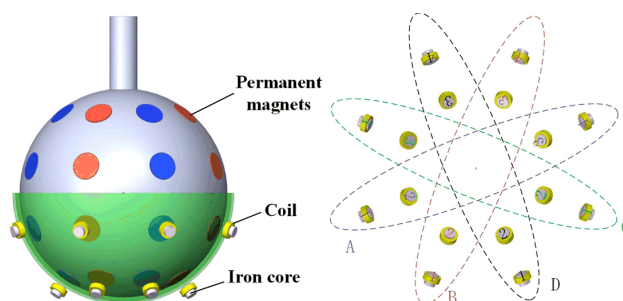**FIGURE 1.** Schematic diagram of the structure of the AMM.

FIGURE 2. Electromagnetic structure of the motor.

gap between the stator and the rotor through the orifice to form an air film flow field. The air film flow field provides the bearing capacity and supports the rotor to run stably. The motor structure is shown in Fig. 1. Table 1 shows the parameters and specifications of AMM.

The rotational motion of the AMM is driven by electromagnetic force, in which the permanent magnets (PM) of the rotor and the stator coils are the electromagnetic structures of the motor, which generate electromagnetic force. There is 32 cylindrical PM (16 N poles and 16 S poles) distributed on the rotor of the motor in 4 rows and 8 columns. NdFeB is selected as the permanent magnet material, as shown in Fig. 2. There are 16 iron cores and energized coils distributed in two rows on the stator shell. The coils are divided into 4 groups (A, B, C, D), and each group is named 1, 2, 3, and 4. The coils are made of copper, as shown in Fig. 2. AMM completes the multi-degree-of-freedom motion of the motor by adjusting the on-off of the coils (1 group to 4 groups).

The motion of the motor is divided into rotation and deflection motion. When the rotor rotates around the Z-axis, the

motor is in rotation mode. At this time, the coils A, B, C, and D groups are fed with current, which generates the same magnetic field as the PM to drive the rotor to move; When the motor deflects around the center plane, it controls the current of No. 1 and No. 2 of the 4 groups of coils to generate the same magnetic field as the PM and controls No. 3 and No. 4 of the four groups of coils to pass currents with the same amplitude and opposite directions, which produces an opposite magnetic field to the PM, which drives the rotor to perform deflection motion.

During the operation of the motor, high-pressure gas is first introduced into the interior of the motor. The gas needs to be filtered to prevent the air from carrying moisture and other impurities from causing damage to the interior of the motor. The high-pressure gas pushes the rotor of the motor into a suspended state and then controls the coil to energize to rotate. During the operation of the motor, gas is continuously introduced, and the gas flow inside the motor can take away the heat generated during the operation, which is equivalent to its cooling effect.

III. RESEARCH ON ELECTROMAGNETIC PROPERTIES

The complex structure of the AMM is the focus of research because the multi-DOF motion is realized by electromagnetic drive from different angles. Using finite element software for electromagnetic analysis can get higher precision results. Maxwell's equation is the basis of electromagnetic field calculation. The electromagnetic equation in a rectangular coordinate system is as follows:

$$\begin{cases} \nabla \times H(x, y, z) = J(x, y, z) \\ \nabla \cdot B(x, y, z) = 0 \end{cases} \quad (1)$$

where $H(x, y, z)$ is the magnetic field strength; $J(x, y, z)$ is the current density; $B(x, y, z)$ is the magnetic flux density.

The PM of the AMM is cylindrical and distributed outside the spherical shell. Radial magnetization is selected in the magnetization method. Under the rectangular scale system, the air gap magnetic field needs to be decomposed:

$$B(x, y, z) = B_X \cdot \vec{X} + B_Y \cdot \vec{Y} + B_Z \cdot \vec{Z} \quad (2)$$

Since the electromagnetic structure of the AMM is a spherical distribution, the coordinate can be decomposed and the magnetic field distribution relationship suitable for the spherical coordinate system can be obtained. Through the decomposition and transformation of the magnetic field, the magnetic field components in the three directions are as follows in the spherical coordinate system:

$$\begin{cases} B_r = [B_x \cos(\varphi) + B_y \sin(\varphi)] \sin(\theta) + B_z \cos(\theta) \\ B_\theta = [B_x \cos(\varphi) + B_y \sin(\varphi)] \cos(\theta) - B_z \sin(\theta) \\ B_\varphi = B_y \cos(\varphi) - B_x \sin(\varphi) \end{cases} \quad (3)$$

The electromagnetic force generated at the air gap acts on the fixed rotor after the rotating magnetic field of the AMM. Since the electromagnetic force has a large component along the diameter direction, the REF is the main factor

affecting the operation of the motor and also the main cause of faults caused by the vibration of the motor. The vibration and noise generated by the motor mainly depend on the value and frequency of electromechanical magnetic force, which is an important research direction to solve the vibration fault. When the rotor rotates in a no-load state, the PM acts alone to produce the REF. The AMM is in a load operation state. The PM magnetic field and the armature reaction generate a magnetic field together to generate a rotating magnetic field and generate synthetic REF. According to the analysis of magnetic field characteristics at the air gap, the force at the position of the stator bulge is as follows:

$$F_r = \frac{1}{2\mu_0} \left(B_R^2 - B_T^2 \right) \quad (4)$$

where F_r is the REF of the multi-DOF motor (N/m^2); B_R and B_T are the radial magnetic flux density (T) and the tangential flux density (T) of the motor air gap.

Since the permeability of ferromagnetic materials is greater than that of vacuum, the tangential flux caused by the magnetic field can be ignored. The magnetic flux of the AMM is mainly composed of two parts: the magnetic flux component generated by the magneto-dynamic force of the PM at the air gap and the magnetic flux component generated by the coupling of the armature reaction at the air gap. Therefore, the REF of the motor can be rewritten as:

$$F_r = \frac{1}{2\mu_0} \left(B_{P\gamma} + B_{S\gamma} \right)^2 = \frac{1}{2\mu_0} B_{P\gamma}^2 + \frac{1}{\mu_0} B_{P\gamma} B_{S\gamma} + \frac{1}{2\mu_0} B_{S\gamma}^2 \quad (5)$$

where μ_0 is the vacuum permeability; $B_{P\gamma}$ is the magneticfluxdensity (T) of the PM magnetomotive force at the air gap; $B_{S\gamma}$ is the magnetic density (T) of the stator armature reaction at the air gap.

According to the coupling of the fixed magnetic field of the PM and the magnetic field generated by the stator armature reaction, the electromagnetic force along the diameter direction is generated in the raised part of the stator of the motor. The REF can be analyzed by analyzing the magnetomotive force generated by the PM and the magnetomotive force generated by the three symmetric currents of the stator armature reaction. The specific expressions of $B_{R\gamma}$ and $B_{S\gamma}$ can be expanded as follows:

$$B_{R\gamma} = \lambda \sum_{m_p} F_{Pm} \cos m_p (\omega t - p\theta) \quad (6)$$

$$B_{S\gamma} = \lambda \sum_{\mu} \sum_{m_S} F_{Sm} \cos \left(\mu\omega t - p m_S \theta - \varphi^S \right) \quad (7)$$

where m_P is the harmonic order of the PM magnetic field; m_S is the harmonic coefficient of the stator armature reaction magnetic field; F_{Pm} is the m_p sub-harmonic magnetomotive force amplitude (A) of the PM; F_{Sm} is m_S harmonic magneto motive force amplitude generated by μ time current of the stator three-phase winding; λ is the equivalent permeance of the motor; θ is the mechanical angle of the rotor space; ω is

the angular frequency of the fundamental current; φ^S is the magnetic force Initial phase.

When calculating the permeance, since the rotor surface of the air-floating multi-DOF model is a smooth surface, taking the centerline of a certain tooth of the stator as the coordinate, the equivalent air-gap permeance of the motor is calculated as:

$$\lambda = \lambda_0 + \sum_{k=1}^{\infty} \lambda_k \cos(k\theta Z_0) \tag{8}$$

where λ_0 is the effective value of air gap permeability (H^{-1}); k is the tooth harmonic order; λ_k is the air gap k-order tooth harmonic permeability (H^{-1}); Z_0 is the stator slot number.

Multiply the magnetic force expression of the PM of the motor by the equivalent air gap magnetic conductivity expression to obtain the magnetic density generated by the PM at the air gap:

$$B_{P\gamma} = \sum_{m_p} B_{Pm} \cos m_p(\omega t - p\theta)$$

$$+ \sum_{k=1}^{\infty} \sum_{m_S} B_{Pmk} \cos[m_P\omega t - (m_P p \pm kZ_0)\theta] \tag{9}$$

where B_{Pm} is the average PM flux density m_P sub-harmonic amplitude (T); B_{Pmk} is the k-order harmonic magnetic flux density amplitude (T) of the PM harmonic magnetomotive force acting on the permanent magnet tooth.

In the same way, multiply the expression of the stator armature reaction magnetomotive force with the equivalent air gap permeability expression to obtain the magnetic density generated by the armature reaction magnetomotive force at the air gap:

$$B_{S\gamma} = \sum_{\mu} \sum_{m_S} B_{Sm} \cos(\mu\omega t - pm_S\theta)$$

$$+ \sum_{k=1}^{\infty} \sum_{\mu} \sum_{m_S} B_{Smk} \cos[\mu\omega t - (pm_S + kZ_0)\theta] \tag{10}$$

where B_{Sm} is the average stator armature response m_S harmonic flux density amplitude (T); B_{Smk} harmonic magnetomotive force acts on the k-order armature response mS harmonic flux density amplitude (T).

Substitute Eq. 9 and Eq. 10 into Eq. 5 to obtain the REF at the stator of the AMM in response to the PM magnetic field and the stator armature.

$$F_r$$

$$= \frac{1}{2\mu_0} \left\{ \begin{array}{l} \sum_{m_p} B_{Pm} \cos m_p(\omega t - p\theta) \\ + \sum_{\mu} \sum_{m_S} B_{Sm} \cos(\mu\omega t - pm_S\theta) \\ + \sum_{k=1}^{\infty} \sum_{m_S} B_{Pmk} \cos[m_P\omega t - (m_P p \pm kZ_0)\theta] \\ + \sum_{k=1}^{\infty} \sum_{\mu} \sum_{m_S} B_{Smk} \cos[\mu\omega t - (pm_S + kZ_0)\theta] \end{array} \right\} \tag{11}$$
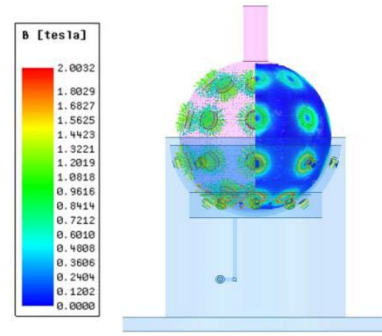

FIGURE 3. Magnetic density cloud diagram and magnetic field vector diagram of AMM at rated speed.

where the first two parts are the REF generated by the coupling of the fundamental wave between the PM and the stator armature, and the second half is the REF generated by the coupling of multiple harmonics between the PM and the stator armature on the stator protrusion.

The finite element calculation method of the motor magnetic field is to transform the marginal conditions in the partial differential equation into an energy generalized function problem, and then discretize it and establish the node as a variable fractional equation for solving, reducing the complexity of the procedure.

In the load analysis of the AMM, the rated speed of the rotor motion is set to 1500rpm, and the excitation source is added to the stator coil winding. The PM of the AMM adopts the radial magnetization method. The magnetization directions of the N pole and the S pole are opposite. The maximum amplitude of magnetic flux density is about 2.00T, which is located near the distance between the magnetic poles of the motor rotor and adjacent to each other. The magnetic flux density between the pole slots is larger. The magnetic density cloud diagram and magnetic field vector diagram of the AMM at the rated speed are shown in Fig. 3. Observation of the magnetic density cloud shows that the permanent magnets are magnetized in radial direction and the magnetic density vector of the circular permanent magnets is radial. The larger magnetic density in the coil corresponding to the rotor part indicates that the motor structure has excellent electromagnetic performance both in the rotating and deflecting states, which proves the feasibility of AMM multi-freedom motion.

Due to the variation of time and space under rated load, the average value of measured magnetic density is relatively small. It can be seen from the right half of Fig. 3 that in the running state of the motor, the magnetic field lines of the permanent magnets are not symmetrically distributed, and the magnetic circuit changes due to the armature reaction. At the corresponding time, both the air gap of the motor and the main magnetic circuit have magnetic fields, but no magnetic flux leakage occurs.

Fig. 4 shows the waveforms of the radial flux density and the tangential flux density of the air gap changing with the
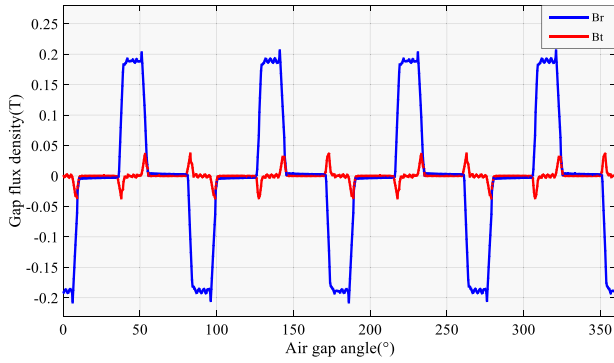
FIGURE 4. Waveforms of radial and tangential magnetic densities under air gap.

circumferential distance when the circumferential distance changes at the air gap of the AMM. The peak value of the radial magnetic density at the air gap of the motor is 0.2015T, and the peak value of the tangential magnetic density is 0.0411T. It is obvious that the radial magnetic density is the main factor of the air gap magnetic density, which is mainly produced by the PM.

The distribution and amplitude of radial force were calculated by finite element software. The analysis shows that the amplitude of REF is large, and the tangential electromagnetic force can be ignored. The research on the change of the REF under the load condition of the AMM is particularly important. After calculation, the FFT decomposition diagram of the REF changing waveform with the horizontal circumferential space and the REF is obtained, as shown in Fig.5.

Fig. 5(a) shows the waveform of the radial force changing with the horizontal circumferential space. The electro- magnetic force at the relative position of the rotor magnetic pole is relatively large, indicating that the REF is the result of the combined effect of PM magnetic field. Fig. 5(b) is the FFT decomposition result of the REF in the motor space. The magnitudes of the 0th-order components and the 16th-order components are the largest, followed by the 32nd-order, 48th-order, 64th-order and 80th-order amplitude components. It can be found that the spatial order with larger amplitude is a multiple of 16 times. In the spatial position, the REF of the AMM is solved, and the distribution diagram of the REF in three-dimensional space is drawn, as shown in Fig. 6.

In Fig. 6, the REF is uniformly distributed in space, the amplitude is the same, and there are 8 symmetrical periods with the same proportion in the circumferential direction, which corresponds to the structure of the PM of the motor in 4 rows and 8 columns. The air gap position of the rotor of the motor is analyzed, and the change of the REF is solved by finite element calculation. The change of the REF with time under different periods is shown in Fig. 7(a). The FFT decomposition is shown in Fig. 7(b).

It can be concluded from Fig. 7 that the maximum REF amplitude is 65.43N, showing periodic changes. Then, the REF is decomposed by FFT, and the amplitude of the radial
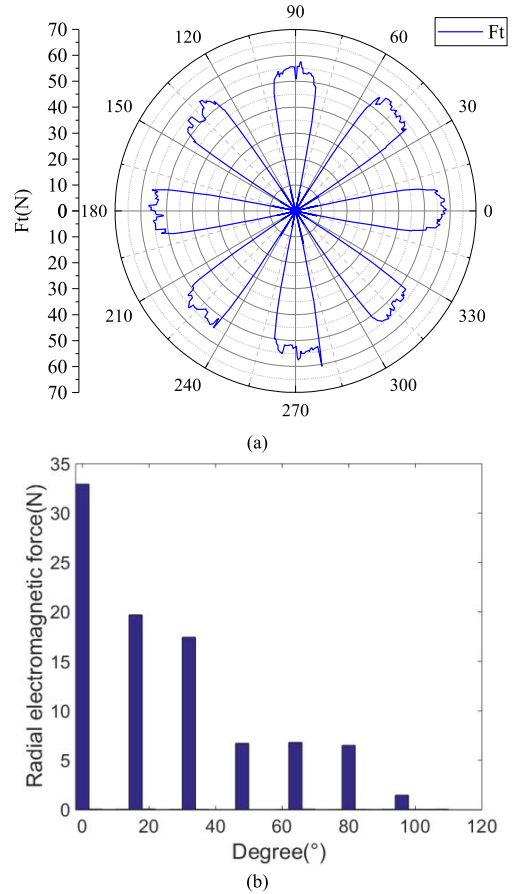

(a)

(b)

FIGURE 5. Schematic diagram of REF. (a) Waveform of REF varying with horizontal circumferential space, (b) FFT decomposition of REF.
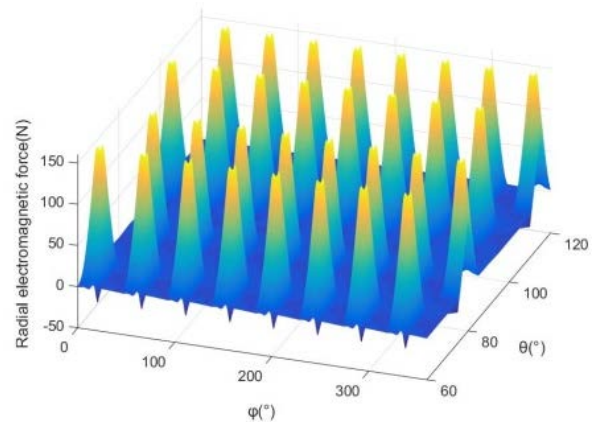

FIGURE 6. Waveform of spatial distribution of REF.

electromagnetic force at different harmonic frequencies can be obtained. The DC component has the largest amplitude component at the frequency of 200 Hz, and the characteristic component that has the greatest impact on vibration is still twice the fundamental frequency. It can be concluded that the amplitude of even multiples such as 2 times, 4 times, 6 times,
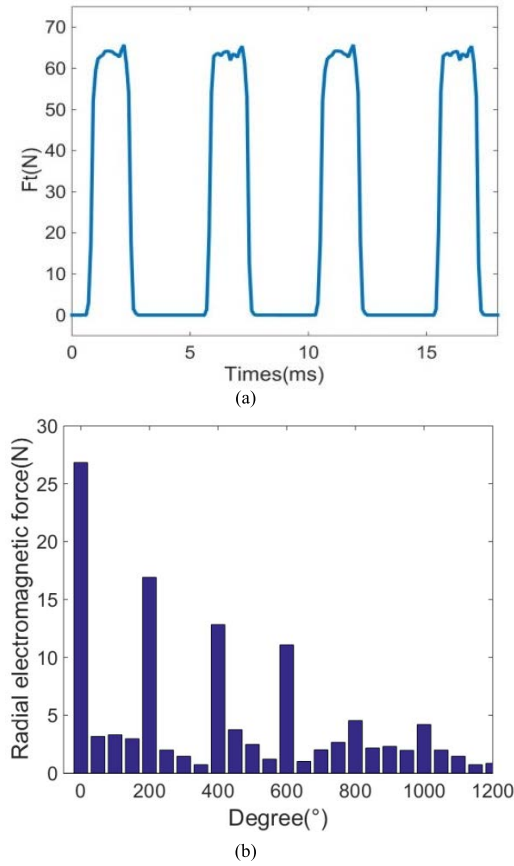
FIGURE 7. Schematic diagram of REF. (a) Waveforms of REF at different time periods, (b) FFT decomposition of the REF.

and 8 times is larger. Relatively speaking, the vibration of these positions will also be relatively large.

Ignoring the special structure of the motor stator teeth and the edge leakage flux, under the same air gap, the REF of different spacings is also different. Compared with different deflection angles and different air gap distances, the magnitude of the electromagnetic force is also different. Through the calculation under different conditions, the comparison curve of the electromagnetic force and the air gap distance under different deflection angles is shown in Fig. 8.

It can be seen from Fig. 8 that the REF is greater under the condition of rotation. With the increase of deflection angle, the REF decreases in varying degrees. Under the same deflection angle, the air gap spacing is inversely proportional to the REF. As the air gap distance decreases, the REF of the rotor also increases. After deflection at different angles, the magnitude of the electromagnetic force also gradually decreases.

By analyzing the electromagnetic force under motor load operation and deflection operation, REF is obtained as the main influence factor of electromagnetic field on motor components. After the frequency decomposition of REF, the main harmonic orders and laws affecting REF are found to guide the following modal analysis.
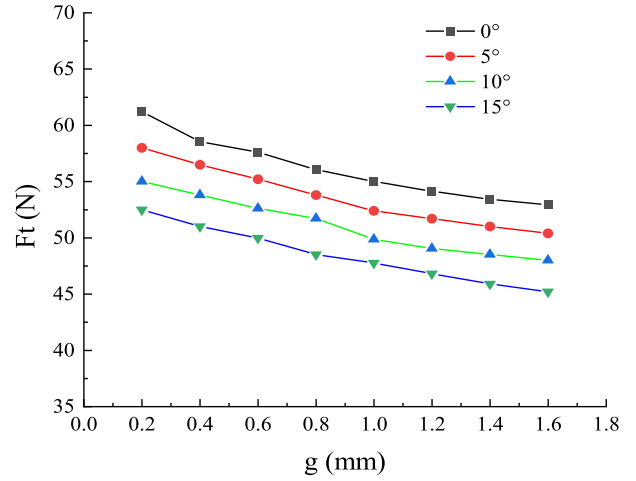

FIGURE 8. Comparison curve of electromagnetic force and air gap distance under different deflection angles.

IV. MOTOR MODAL ANALYSIS
A. MODAL ANALYSIS THEORY
The modal analysis of the motor is helpful to test the stability of the motor. Through modal simulation, the deformation of AMM at different frequencies can be obtained; by summarizing the deformation at different frequencies, the occurrence of resonance can be effectively avoided. Since AMM can realize multi-directional rotational motion, it is necessary to deduce the equation of motion. According to the theory of elasticity, the equation of motion system of AMM is deduced, and its matrix equation can be expressed as:

$$Mx'' + Cx' + Kx = Q(t) \qquad (12)$$

Since Among them, M is the mass matrix, C is the damping matrix, K is the stiffness matrix; x'' is the acceleration, x' is the velocity vector; x is the displacement vector; $Q(t)$ is the system load.

AMM can realize rotation and deflection during operation. When the rotor rotates with the Z axis as the center line, only the displacement and force of the X and Y axes need to be analyzed. Deriving Eq. (12), the forces in two directions are obtained:

$$\begin{cases} F(x) = m\dfrac{d^2x(t)}{dt^2} + c_n\dfrac{dx(t)}{dt} + c_r\left[\dfrac{dx(t)}{dt} + \Omega y(t)\right] + kx(t) \\ F(y) = m\dfrac{d^2y(t)}{dt^2} + c_n\dfrac{dy(t)}{dt} + c_r\left[\dfrac{dy(t)}{dt} + \Omega x(t)\right] + ky(t) \end{cases}$$
$$(13)$$

where Ω is the rotational speed of the rotor; m is the mass of the rotor; k is the stiffness of the rotor bearing; c_n is the external damping of the rotor system; c_r is the internal damping of the rotor system; $x(t)$, $y(t)$, $F(x)$, $F(y)$ are the displacement in different directions and the excitation force of the structure, respectively.

When the motor rotor is deflecting, it is necessary to analyze the displacement and force of the three degrees of freedom, X, Y, and Z. Eq. (12) is deduced to obtain the force
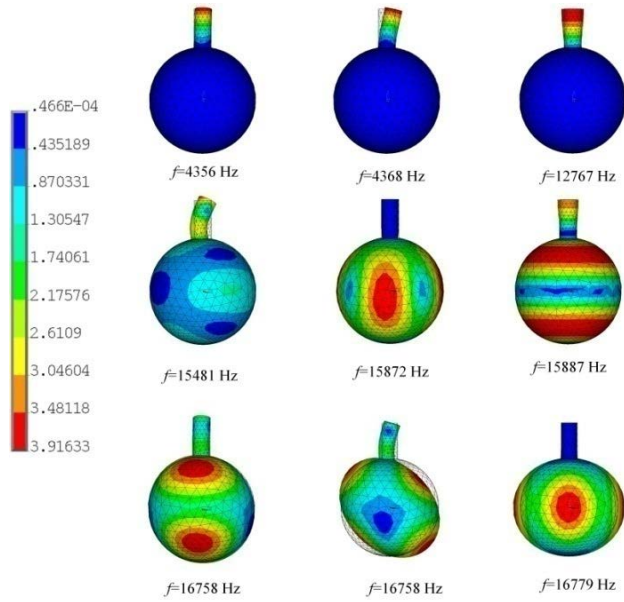
FIGURE 9. Cloud diagram of rotor modal analysis.

TABLE 2. Paramenters of rotor material.

Material	Elastic Modulus Pa	Poisson's ratio	Density kg/m^3
Steel	2.06E+11	0.3	7800
Rubidium Iron Boron	1.5E+11	0.24	7400

FIGURE 10. The modal cloud diagram of the stator under the aluminum material.

in three directions:

$$\left\{ \begin{array}{c} F(x) \\ F(y) \\ F(z) \end{array} \right\} = \left(\begin{array}{ccc} k_{xx} & k_{xy} & k_{xz} \\ k_{yx} & k_{yy} & k_{yz} \\ k_{zx} & k_{zy} & k_{zz} \end{array} \right) \left\{ \begin{array}{c} x \\ y \\ z \end{array} \right\} + \left(\begin{array}{ccc} c_{xx} & c_{xy} & c_{xz} \\ c_{yx} & c_{yy} & c_{yz} \\ c_{zx} & c_{zy} & c_{zz} \end{array} \right) \left\{ \begin{array}{c} x' \\ y' \\ z' \end{array} \right\} \quad (14)$$

B. ANALYSIS OF MODAL CHARACTERISTICS

The AMM structure is composed of a stator and a rotor. The modal of the rotor is analyzed, and 32 cylindrical permanent magnets are embedded on the rotor. When modal simulation of AMM is performed, no force and constraint conditions are added to the motor, and the deformation of the motor at the natural frequency is observed. During the analysis, the permanent magnets and spherical rotor are glued together to form a whole. The motor rotor is meshed, and then solved, and the modal changes of the motor at different frequencies are obtained.

1) MODAL DEFORMATION ANALYSIS OF ROTOR

The rotor is the basic structure of the AMM. Establishing a suitable three-dimensional model of the rotor is helpful to accurately analyze the modal of the rotor. The PM on the rotor are embedded in the rotor casing, and small gaps and small parts are ignored. The influence of modal analysis, spherical rotor material and permanent magnet material parameters are shown in Table 2. The deformation of the rotor at different frequencies is analyzed through simulation, and the modal change cloud diagram is shown in Fig 9.

Deformation of the motor rotor begins at the output shaft position. As the frequency increases, the overall rotor begins to deform. The deformation of the rotor is about $l = 3.8$, and

the deformation gradually decreases. The modal frequency mainly distributed in the range of $f = 15000Hz$ to $f = 16000Hz$, the deformation is relatively small, and the deformation of the rotor is about $l = 0.45$ on average. In order to avoid resonance affecting the stability of the motor, the frequency range around $f = 4356Hz$ and $f = 12767Hz$ should be avoided, select the frequency range from $f = 4500Hz$ to $f = 12500Hz$ as a relatively ideal vibration frequency range.

2) STATOR MODAL DEFORMATION ANALYSIS

Import the established stator model into finite element for modal analysis, obtain the deformation diagram of the motor at different frequencies through calculation, observe the deformation of the motor in each frequency range, and do not set constraints and boundary conditions in the process of simulation analysis, carry out modal analysis on the stator casing of the motor, select the modal under 9 frequencies of the stator for analysis, and obtain the deformation variables and deformation cloud diagrams at different frequencies, as shown in Table 3 and Fig. 10.

Through the modal analysis of the stator under the aluminum material, the relationship between the modal frequency and the deformation of the stator can be obtained. When the frequency of the stator continues to increase, the deformation of the stator increases and decreases in stages, which helps to shield the frequency under large deformation, reduces the amount of deformation of the motor, and helps to enhance the stability of the motor. In the frequency range from $f = 6465Hz$ to $f = 8446Hz$, the deformation increases

TABLE 3. Deformation of aluminum stator.

Parameter	Value		
Frequency f/Hz	4651	6465	7165
Deformation	0.95	0.5	1.5
Frequency f/Hz	7254	7761	8446
Deformation	1.13	1.23	1.73
Frequency f/Hz	8790	9475	9671
Deformation	0.77	0.53	1.24

TABLE 4. Parameters under three under three material.

Material	Elastic Modulus Pa	Poisson's ratio	Density kg/m^3
Steel	2.06E+11	0.3	7800
Aluminum	0.72E+11	0.33	2810
Stainless steel	1.94E+11	0.3	7930

FIGURE 11. Modal cloud diagram of stator under steel material.

FIGURE 12. The modal cloud diagram of the stator under stainless. steel material.

continuously, from the deformation $l = 0.497$ to $l = 1.73$, and in the frequency range from 8790 Hz to 9671Hz, the deformation increases from $l = 0.778$ to $l = 1.246$, in order to avoid resonance affecting the stability of the motor, the frequency range near the frequency range f=8446Hz and $f = 9671$Hz should be avoided, and the frequency range $f = 6445$Hz and $f = 8790$Hz should be selected as relatively ideal vibration frequency ranges.

In order to further explore the resonance and deformation of the AMM stator, two different materials were listed for comparative analysis, and the fixed frequency and deformation of the stator under different materials were obtained, which provided guidance for the selection of motor stator materials. The material properties are shown in Table 4.

Next, the deformation conditions under different materials are solved by simulation, and the deformation diagrams under the materials are compared to obtain the deformation conditions under the three materials. Under different materials, to ensure that other conditions are the same, the two materials of aluminum and stainless steel are respectively input to solve, and the deformation cloud diagram of the stator under the two materials is obtained. As shown in Fig. 11 and Fig. 12.

It can be seen from the deformation of the two materials, steel and stainless steel, that the deformation trend of the stator is basically the same, but the deformation of the stator is lower than that of the aluminum material. In order to see the comparison of the three materials more clearly, made a histogram for analysis, as shown in Fig. 13.

By comparing and analyzing the simulation results of Fig.10 to Fig. 12, it can be clearly seen that the deformation distribution of the stator in different frequency segments, under the frequency segment f=5000-6000Hz, there is no stator deformation, the structure is stable, and the frequency The segment f=9000-10000Hz has a large deformation, and the AMM should avoid this frequency segment during the actual rotation process. On this basis, it can be seen that
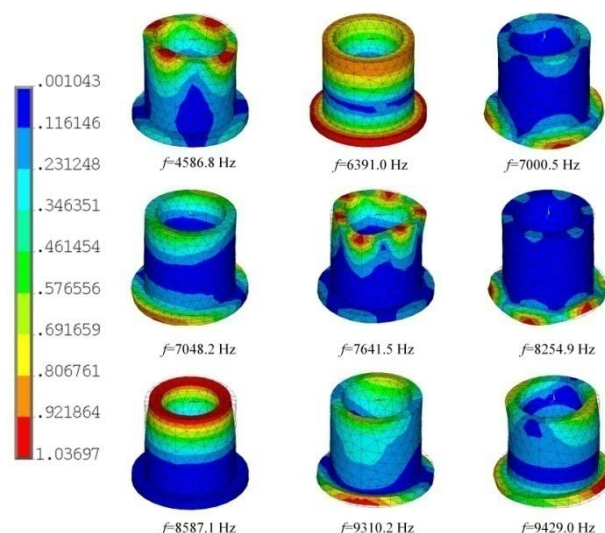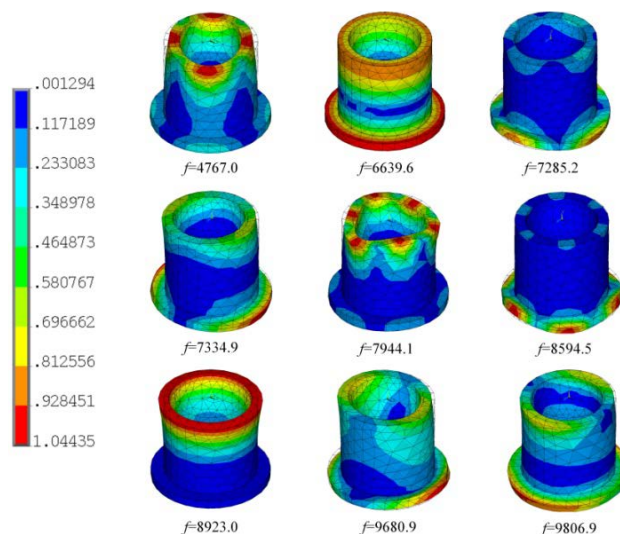
the deformation of the aluminum material is the largest, and the deformation is close to 2, which is not suitable for the stator material of the motor. In contrast, the deformation of the two steel structures is very small, and the deformation is 1.1, which is almost one smaller than that of the aluminum material. It is more suitable for the stator material of the motor, which is helpful for the stability of the motor when it moves with multiple degrees of freedom.

C. EXPERIMENTAL RESULTS AND ANALYSIS

The generation of vibration will inevitably have an adverse effect on the operation of the motor, so it is very necessary to conduct experiments on the vibration characteristics of the designed AMM. The experimental platform includes AMM motor device and detection and control equipment. The detection and control equipment includes the host computer, power
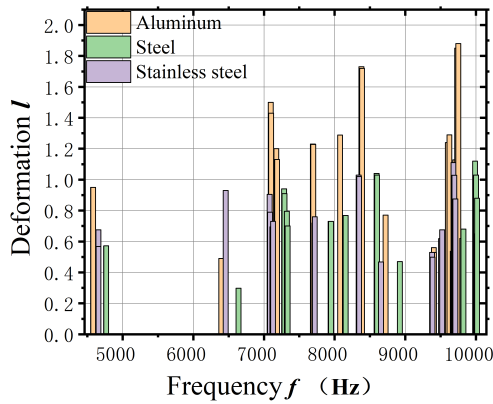
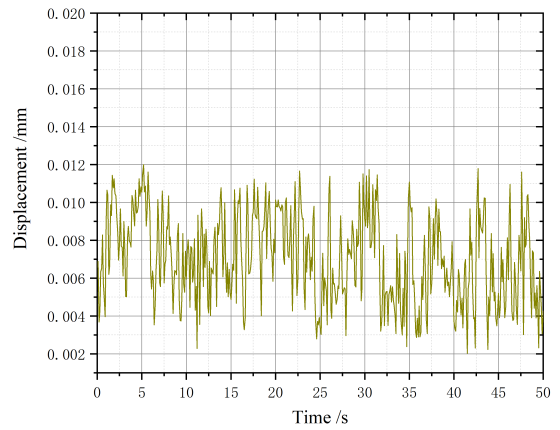**FIGURE 13.** Modal distribution diagrams for three materials.

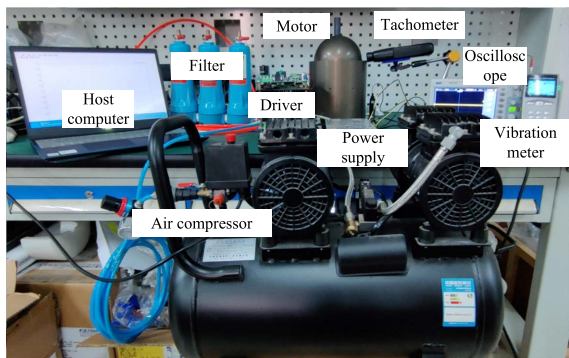**FIGURE 14.** Vibration experiment platform of air-floating multi-DOF motor.

FIGURE 15. Vibration displacement diagram of AMM.

FIGURE 16. Schematic diagram of vibration of base and stator.

supply, control board, vibration meter TIME7231, and speed meter, as shown in Fig. 14.

The probe of the vibrometer TIME7231 is attached to the base and stator housing of the AMM, and a piezoelectric sensor is used to convert the vibration signal into an electrical signal. By processing and analyzing the input signal, the peak acceleration, peak displacement, or real-time spectrogram of the vibration measurement is obtained. The acceleration frequency range is 10Hz-10kHz and the displacement frequency range is 10Hz-500Hz, where the acceleration measurement range is 1-390m/s^2 and the displacement measurement range is 0.01-8mm. In the testing process, the red dot on the front of the LEMO plug of the vibration measurement probe is aligned with the red dot on the LEMO socket and inserted into the plug to start the measurement work. The measurement spectrum is displayed in real-time and the test data is stored using the storage function of the vibrometer. The collected vibration data is then fitted to a curve, and the results are shown in Fig. 15 and Fig. 16.

During the operation of the AMM, it can be seen by the change of vibration displacement of the motor base that there is a certain vibration of the motor base, but the maximum vibration does not exceed 0.12 mm, and the motor operation process is basically stable, and the vibration amplitude is significantly reduced compared with
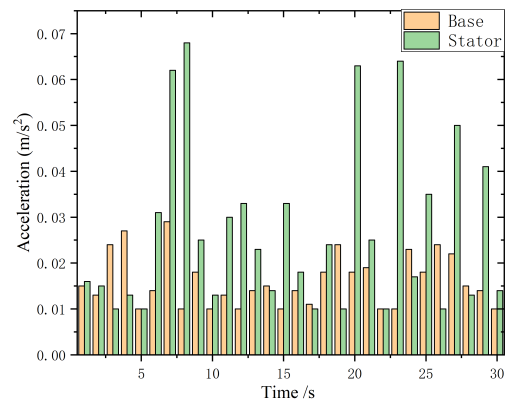
the multi-degree-of-freedom motor based on liquid support. Fig. 16 shows the vibration of the base and stator during the motor motion. The analysis shows that the base and stator vibrations are basically the same, and the relative deformation of the stator shell is larger, which is caused by the support between the stator and rotor during the motion of the AMM. The experimental results provide verification of the simulation results. When improving the motor at a later stage, the stator shell should be reinforced to reduce the vibration of the motor by increasing the thickness of the stator shell to achieve the purpose of stable operation of the motor.

V. CONCLUSION

In this paper, the structure of the gas floating multi-degree-of-freedom motor is proposed based on the multi-degree-of-freedom permanent magnet motor, and the bearing structure of the motor is optimized. Based on the gas-bearing, the mechanical friction of the motor is greatly reduced. In the article, the analytical settlement and the modal analysis of the vibration state of the motor stator and rotor are carried out for the complex electromagnetic force distribution of the AMM.

The main contributions of this paper are as follows.

1) In this paper, the electromagnetic distribution and structural forces of AMM are analyzed by modeling with Maxwell's equations. The electromagnetic forces under rated load are calculated and decomposed for the state of AMM with gas-lubricated support. Through the frequency decomposition of the electromagnetic force and introducing the structure and mathematical model of the hydrostatic gas bearing, the influence of the electromagnetic field loading force on the stator is analyzed, and the REF is concluded as the main cause of the deformation of the motor stator.

2) In this paper, the magnetic density cloud and magnetic field vector diagram at the rated speed of AMM is analyzed by finite element calculation. The waveform of REF with horizontal circular space is solved, the frequency decomposition of the waveform is carried out, the harmonic distribution law for REF is derived, and the deflection movement of the motor is analyzed for REF under the deflection state of AMM, and the electromagnetic force variation law under the deflection angle and different air gap spacing is summarized.

3) The natural frequency of the motor stator is analyzed by finite element software. Then the influence of stator material on the modal analysis was explored, and it was found that the stator deformation was minimal under aluminum material, and there was no deformation of stator and rotor in the frequency range $f = 5000\text{-}6000\text{Hz}$, which provided help to optimize the structure of AMM.

Finally, the vibration experimental platform of AMM was built, and through the experiment, the vibration of the motor under rated load was measured, and it was verified that AMM can complete the rotation and deflection operation excellently.

REFERENCES

[1] D. K. Kim, H. Yoon, W. Y. Kang, Y. B. Kim, and H. T. Choi, "Development of a spherical reaction wheel actuator using electromagnetic induction," *Aerosp. Sci. Technol.*, vol. 39, pp. 86–94, Dec. 2014.

[2] H. Y. Kim, H. Kim, D. Gweon, and J. Jeong, "Development of a novel spherical actuator with two degrees of freedom," *IEEE/ASME Trans. Mechatronics*, vol. 20, no. 2, pp. 532–540, Apr. 2015.

[3] K. Bai, K.-M. Lee, J. Cao, R. Xu, and L. Li, "Design and decoupled compensation methods of a PM motor capable of 6-D force/torque actuation for minimum bearing reaction," *IEEE/ASME Trans. Mechatronics*, vol. 22, no. 5, pp. 2252–2264, Oct. 2017.

[4] Z. Li and Q. Wang, "Levitation mechanism and improvements of 3-DOF deflection type PM actuator," *IEEE Trans. Appl. Supercond.*, vol. 26, no. 7, pp. 1–5, Oct. 2016.

[5] S. Cho, J.-S. Lim, Y. J. Oh, G. Jeong, D.-W. Kang, and J. Lee, "A study on output characteristics of the spherical multi-DOF motor according to the number of phases and pole pitch angles," *IEEE Trans. Magn.*, vol. 54, no. 11, pp. 1–5, Nov. 2018.

[6] R. Zhou, G. Li, Q. Wang, J. He, and T. Wang, "Drive current calculation and analysis of permanent magnet spherical motor based on torque analytical model and particle swarm optimization," *IEEE Access*, vol. 8, pp. 54722–54729, 2020.

[7] Z. Li, X. Yu, X. Wang, and X. Xing, "Optimization and analysis of cogging torque of permanent magnet spherical motor," *IEEE Trans. Appl. Supercond.*, vol. 31, no. 8, pp. 1–5, Nov. 2021.

[8] W. Ma, J. Cui, Y. Liu, and J. Tan, "Improving the pneumatic hammer stability of aerostatic thrust bearing with recess using damping orifices," *Tribol. Int.*, vol. 103, pp. 281–288, Nov. 2016.

[9] C. Kang, K. Jung, M. Lee, and G. Jang, "Finite-element coupled analyses of the Reynolds and Hagen–Poiseuille equations to calculate pressure and flow of fluid dynamic bearings with a recirculation channel," *Tribol. Int.*, vol. 128, pp. 52–64, Dec. 2018.

[10] T. Gustafsson, K. R. Rajagopal, R. Stenberg, and J. Videman, "An adaptive finite element method for the inequality-constrained Reynolds equation," *Comput. Methods Appl. Mech. Eng.*, vol. 336, pp. 156–170, Jul. 2018.

[11] Y. Chai and J. Ouyang, "Appropriate stabilized Galerkin approaches for solving two-dimensional coupled Burgers' equations at high Reynolds numbers," *Comput. Math. Appl.*, vol. 79, no. 5, pp. 1287–1301, Mar. 2020.

[12] I. Arregui, J. J. Cendán, and M. González, "A local discontinuous Galerkin method for the compressible Reynolds lubrication equation," *Appl. Math. Comput.*, vol. 349, pp. 337–347, May 2019.

[13] L. Zheng, H. Wei, L. Lingqi, and W. Qunjing, "Calculation and optimization of a permanent magnetic hybrid driven 3-DOF motor," *Int. J. Appl. Electromagn. Mech.*, vol. 58, no. 2, pp. 121–155, Aug. 2018.

[14] Y. Sakaidani, K. Hirata, and N. Niguchi, "Characteristics analysis of a 2-D differentially coupled magnetic actuator," *IEEE Trans. Magn.*, vol. 52, no. 3, pp. 1–4, Mar. 2016.

[15] A. Looser, A. Tüysüz, C. Zwyssig, and J. W. Kolar, "Active magnetic damper for ultrahigh-speed permanent-magnet machines with gas bearings," *IEEE Trans. Ind. Electron.*, vol. 64, no. 4, pp. 2982–2991, Apr. 2017.

[16] A. Tüysüz, C. Zwyssig, and J. W. Kolar, "A novel motor topology for high-speed micro-machining applications," *IEEE Trans. Ind. Electron.*, vol. 61, no. 6, pp. 2960–2968, Jun. 2014.

[17] K. Hikichi, S. Togo, M. Esashi, and S. Tanaka, "Hydroinertia gas bearing for ultra-small gas turbine engine: Influence of operating temperature for characteristic of hydroinertia gas bearing," *Toraibarojisuto/J. Jpn. Soc. Tribol.*, vol. 55, no. 4, pp. 292–299, 2010.

[18] V. I. Grabovskii, "Optimum gas journal bearing with open bearing ends and feeder slot," *Fluid Dyn.*, vol. 39, no. 4, pp. 540–550, Jul. 2004.

[19] C. Zhang, H. Ao, and H. Jiang, "Static and dynamic bearing performances of hybrid gas dynamic bearings," *Tribol. Int.*, vol. 160, Aug. 2021, Art. no. 107036.

[20] X. Fang and H. Liu, "Measuring micro-friction torque in MEMS gas bearings," *Sensors*, vol. 16, no. 5, pp. 726–740, 2016.

[21] Q. Liu, S. Zhang, Y. Li, G. Lei, and L. Wang, "Hybrid gas-magnetic bearings: An overview," *Int. J. Appl. Electromagn. Mech.*, vol. 66, no. 2, pp. 313–338, Jun. 2021.

[22] L. S. Andrés and T. H. Kim, "Thermohydrodynamic analysis of bump type gas foil bearings: A model anchored to test data," *J. Eng. Gas Turbines Power*, vol. 132, no. 4, pp. 042504–042514, Apr. 2010.

[23] Y. Guangwei, G. Weiping, D. Jianjun, and L. Tun, "Numerical analysis of spiral grooved opposed-hemisphere gas bearings: A parametric study," *Proc. Inst. Mech. Eng. J, J. Eng. Tribol.*, vol. 230, no. 8, pp. 930–943, Aug. 2016.

[24] K. Takahara, K. Hirata, N. Niguchi, Y. Nishiura, and Y. Sakaidani, "Experimental evaluation of the static characteristics of multi-degree-of-freedom spherical actuators," *IEEE Trans. Magn.*, vol. 53, no. 11, pp. 1–5, Nov. 2017.

[25] C. Jia, H. Zhang, S. Guo, M. Qiu, W. Ma, and Z. Zhang, "Study on dynamic characteristics of gas films of spherical spiral groove hybrid gas bearings," *Proc. Inst. Mech. Eng. J, J. Eng. Tribol.*, vol. 233, no. 8, pp. 1169–1181, Aug. 2019.

[26] Z. Xing, W. Zhao, X. Wang, and Y. Sun, "Reduction of radial electromagnetic force waves based on PM segmentation in SPMSMs," *IEEE Trans. Magn.*, vol. 56, no. 2, pp. 1–7, Feb. 2020.

[27] W. Liang, J. Wang, P. C.-K. Luk, and W. Fei, "Analytical study of stator tooth modulation on electromagnetic radial force in permanent magnet synchronous machines," *IEEE Trans. Ind. Electron.*, vol. 68, no. 12, pp. 11731–11739, Dec. 2021.

[28] H. Yang and Y. Chen, "Influence of radial force harmonics with low mode number on electromagnetic vibration of PMSM," *IEEE Trans. Energy Convers.*, vol. 29, no. 1, pp. 38–45, Mar. 2014.

[29] H.-W. Cho, K.-J. Ko, J.-Y. Choi, H.-J. Shin, and S.-M. Jang, "Rotor natural frequency in high-speed permanent-magnet synchronous motor for turbo-compressor application," *IEEE Trans. Magn.*, vol. 47, no. 10, pp. 4258–4261, Oct. 2011.

[30] Z. Xing, X. Wang, and W. Zhao, "Research on weakening measure of radial electromagnetic force waves in permanent magnet synchronous motors by inserting auxiliary slots," *IET Electr. Power Appl.*, vol. 14, no. 8, pp. 1381–1395, Aug. 2020.

ZHENG LI (Member, IEEE) was born in Shijiazhuang, Hebei, China, in 1980. He received the B.Sc. and Ph.D. degrees in electrical engineering and power electronics and electric drive from the Hefei University of Technology, Hefei, in 2002 and 2007, respectively.

From July 2013 to July 2014, he has been a Visiting Scholar and a part-time Faculty Member of the College of Engineering, Wayne State University, USA. Since 2007, he has been a Lecturer, an Associate Professor, and a Professor with the School of Electrical Engineering, Hebei University of Science and Technology. He is the author of more than 300 published papers. His current research interests include design, analysis, control of novel motors and actuators, intelligent control, and power electronics. He is an Active Reviewer of the IEEE TRANSACTIONS ON INDUSTRIAL ELECTRONICS, IEEE TRANSACTIONS ON ENERGY CONVERSION, and IEEE TRANSACTIONS ON MAGNETICS AND ELECTRIC POWER COMPONENTS AND SYSTEMS.

LIBO LIU was born in Baoding, China, in 1997. He received the B.Sc. degree in electrical engineering and automation from the Shaanxi University of Science and Technology, China, in 2020. He is currently pursuing the master's degree with the Hebei University of Science and Technology.

His research interest includes multi-DOF motor design and control.

XUANXUAN XING was born in Shijiazhuang, China, in 1995. He received the bachelor's degree in electrical engineering and automation from the Hebei University of Science and Technology, in 2019, where he is currently pursuing the master's degree.

His research interests include the design and optimization of multi-degree-of-freedom motors.

ZHIBANG YAN was born in Handan, China, in 1999. He received the bachelor's degree in electrical engineering and automation from Hebei Normal University, in 2017. He is currently pursuing the master's degree with the Hebei University of Science and Technology.

He is currently a Graduate Student with the Hebei University of Science and Technology. His research interests include special motor control and motor drive.

YU LIU was born in Shijiazhuang, Hebei, China, in 1998. She received the bachelor's degree in electrical engineering and automation from the Hebei University of Science and Technology in 2021, where she is currently pursuing the master's degree.

She is currently a Graduate Student with the Hebei University of Science and Technology. Her research interest includes air float multi-degree-of-freedom motor.

HEXU SUN (Senior Member, IEEE) received the Ph.D. degree in automation from Northeastern University, Shenyang, China, in 1993. He has been a Professor with the School of Control Science and Engineering, Hebei University of Technology, Tianjin, China, and the School of Electrical Engineering, Hebei University of Science and Technology, Shijiazhuang, China. He has authored five books and more than 130 journals and conference papers, and holds 13 U.S. patents and five computer software copyrights. His current research interests include robotics and complex engineering systems. He was a recipient of many prestigious national awards from China. He has been the director in many societies and committees in China. He is currently an invited plenary speaker and the general co-chair of many international conferences.

• • •